Gyrokinetic Simulation of Ion Temperature Gradient Driven Turbulence in 3D Toroidal Geometry

S. E. Parker, W. W. Lee, and R. A. Santoro
Princeton Plasma Physics Laboratory, Princeton University, P.O. Box 451, Princeton, New Jersey 08543

(Received 22 April 1993)

Results from a fully nonlinear three-dimensional toroidal electrostatic gyrokinetic simulation of the ion temperature gradient instability are presented. The model has adiabatic electrons and the complete gyrophase-averaged ion dynamics, including trapped particles. Results include the confirmation of the radially elongated ballooning mode structure predicted by linear theory, and the nonlinear saturation of these toroidal modes. The ensuing turbulent spectrum retains remnants of the linear mode structure, and has very similar features as recent experimental fluctuation measurements.

PACS numbers: 52.35.Ra, 52.25.Gj, 52.35.Qz

Recent advances in both nonlinear δf methods for gyrokinetic simulation [1,2] and massively parallel supercomputing now make it possible to simulate a sizable fraction of a tokamak plasma using realistic physical parameters. Here, we report results from the first whole cross section three-dimensional (3D) electrostatic toroidal gyrokinetic simulation. We investigate the nonlinear evolution of the ion temperature gradient (ITG) driven instability and the associated turbulence and transport in realistic geometry and dimensionality. The ITG mode has long been considered a plausible candidate to explain the observed anomalous ion heat transport in tokamak plasmas, which is substantially above the predicted neoclassical values [3,4]. The simulation results presented below show very similar features in terms of the fluctuation spectrum as the recent beam emission spectroscopy (BES) diagnostic on TFTR [5].

In these simulations, the ions are fully gyrokinetic, including trapped particles. The electrons are treated as adiabatic which permits a moderate size time step (simulations with kinetic electrons are feasible, but the time step would need to be smaller by the factor v_{te}/v_{ti}). The simulation is running efficiently on massively parallel supercomputers (currently the CM-200 and CM-5) which allow simulations of relatively large systems (e.g., $a \gtrsim 100\rho_i$ minor radius, $\Delta x \approx \rho_i$). Typical runs up to this point have used 10^6 to 10^7 particles with 1 to 2 particles per grid cell, and a timing of 2–3 μs per particle per time step on a fully configured CM-200. Fine grid resolution is needed in the toroidal direction because the mode structure is helical (elongated along the magnetic field lines, i.e., $k_\parallel \ll k_\perp$), resulting in a smaller number of particles per grid cell relative to conventional slab simulations.

Starting with the electrostatic gyrokinetic equations with a nonuniform equilibrium **B** field [6], we write $f(\mathbf{z},t) = f_0(\mathbf{z}) + \delta f(\mathbf{z},t)$, where $\mathbf{z} = (\mathbf{R}, v_\parallel, \mu)$, and expand $\dot{\mathbf{z}}$ into its equilibrium and perturbed parts: $\dot{\mathbf{z}} = \dot{\mathbf{z}}^0 + \dot{\mathbf{z}}^1$. $f_0(\mathbf{z})$ is a Maxwellian and satisfies $\dot{\mathbf{z}}^0 \partial_{\mathbf{z}} f_0(\mathbf{z}) = 0$. The equation for the perturbed ion distribution function δf is then [1]

$$\partial_t \delta f + \dot{\mathbf{z}}\,\partial_{\mathbf{z}} \delta f = -\dot{\mathbf{z}}^1 \partial_{\mathbf{z}} f_0 , \qquad (1)$$

where the magnetic moment μ is time independent and the other equilibrium and perturbed phase space variables are evolved using

$$(\dot{\mathbf{R}}^0, \dot{v}_\parallel^0) = \left(-v_\parallel \hat{\mathbf{b}}^* + \frac{\mu}{B}\hat{\mathbf{b}} \times \nabla B, \hat{\mathbf{b}}^* \cdot \mu \nabla B\right) , \qquad (2)$$

$$(\dot{\mathbf{R}}^1, \dot{v}_\parallel^1) = \left(\frac{\hat{\mathbf{b}}}{B} \times \nabla \bar{\phi}, -\hat{\mathbf{b}}^* \cdot \nabla \bar{\phi}\right) , \qquad (3)$$

where $\hat{\mathbf{b}}^* \equiv \hat{\mathbf{b}} + (v_\parallel / B)\hat{\mathbf{b}} \times \hat{\mathbf{b}} \cdot \nabla \hat{\mathbf{b}}$, $\bar{\phi}$ is the gyrophase-averaged electrostatic potential, and dimensionless gyrokinetic units are used $R/\rho_s \to R$, $v_\parallel / c_s \to v_\parallel$, $e\bar{\phi}/T_e \to \bar{\phi}$, $\Omega_i t \to t$, $B/B_0 \to B$, B_0 is a reference value of B, $\mu = (v_\perp / c_s)^2 / (2B/B_0)$, $\Omega_i = eB_0 / m_i c$, $c_s = \sqrt{T_e / m_i}$, and $\rho_s = c_s / \Omega_i$.

The particles follow their fully nonlinear trajectories, δf is represented by $B\delta f(\mathbf{z},t) = \sum_i w_i \delta(\mathbf{z} - \mathbf{z}_i)$, and particle weight w_i is then evolved using [1]

$$\dot{w}_i = -(1 - w_i) \left[\dot{\mathbf{z}}^1 \frac{\partial_{\mathbf{z}} f_0}{f_0}\right]_{\mathbf{z} = \mathbf{z}_i, t} . \qquad (4)$$

Electromagnetic equations have been formulated [1], but not yet implemented in the code. Equations (2) and (3) are similar to those of Hahm [6], and accurate to the same order, but we have assumed $B^* = B$ for numerical efficiency. As usual, finite size particles are used in the configuration space. The electrons are assumed adiabatic ($\delta n_e / n_0 = e\phi / T_e$). This model predicts negligible particle transport and is probably inappropriate at the plasma edge [7]. However, this assumption may be appropriate for predicting core ion heat transport when $L_T / L_n \gg 1$ [8–10].

The simulation coordinates (x, y, ψ) are related to the usual toroidal coordinates (r, θ, ψ) through $x = r\cos\theta$ and $y = r\sin\theta$. Using these coordinates, assuming $(k_\parallel / k_\perp) B_\theta / B_\psi \ll 1$, where B_θ and B_ψ are the poloidal and toroidal components of **B**, one can transform the electrostatic field equation [11] to obtain

$$(T_e/T_i)[1 - \Gamma_0(\mathbf{k}_\perp^2 T_i / T_e)]\phi(\mathbf{k}_\perp, \psi) = \delta\bar{n}_i(\mathbf{k}_\perp, \psi) - \phi(\mathbf{k}_\perp, \psi) , \qquad (5)$$

where $\delta\bar{n}_i = (\bar{n}_i - n_0)/n_0$, $\bar{n}_i$ is the gyrophase-averaged ion

0031-9007/93/71(13)/2042(4)$06.00

density, $\mathbf{k}_\perp = (k_x\rho_s, k_y\rho_s)$, and higher order terms have been neglected. ρ_s is assumed constant in Eq. (5). For the radial boundary condition we set $\delta\bar{n}_i$ to zero for $r \geq a - 4\rho_s$ within the square cross section. The magnetic field is fixed and specified by $B_\psi = B_0R_0/R$, $B_\theta = rB_\psi/R_0q(r)$, and $q(r) = q_0 + \Delta q(r/a)^2$. Initial equilibrium density and temperature profiles are used such that $L_n^{-1} \equiv |\nabla n|/n$ and $L_T^{-1} \equiv |\nabla T|/T$ have a radial variation proportional to $\mathrm{sech}^2[(r-r_0)/l]$, where r_0 and l as well as the peak normalized gradients $L_n^{-1}(r_0)$ and $L_T^{-1}(r_0)$ are all specified parameters. For the results presented, the particles are loaded homogeneously and the variation in the profile appears only in the right-hand side of Eq. (4).

We will now discuss simulation results from a run using the following numerical parameters: 10^6 particles, a $128 \times 128 \times 64$ grid in (x, y, ψ), with a perpendicular grid cell size $\Delta x = \Delta y = \rho_s$, and a time step of $\Delta t c_s/L_T(r_0) = 0.45$. The physical parameters are $\epsilon_T \equiv L_T(r_0)/R_0 = 0.075$, $1/L_n(r_0) = 0$, $T_i = T_e$, $a = 64\rho_s$, and $R_0 = 892\rho_s$, $q_0 = 1.25$, $\Delta q = 3$, $l = 20\rho_s$, $r_0 = \frac{1}{2}a$, $q(r_0) = 2$, $\hat{s} \equiv (r/q)dq/dr = 0.75$ at r_0. The local parameters at $r = r_0$ are similar to the TFTR perturbed supershot experiment [12], except for the aspect ratio. In the initial phase of the run, we observe a clean linear growth of the most unstable toroidal harmonic and the associated 2D eigenmode in (r, θ) with a ballooning type mode structure. Figures 1(a) and 1(b) are the poloidal and toroidal slices of the potential in the linear phase. Figure 1(c) shows the relative amplitude of the various (m,n) modes in the linear phase at the $q = 2$ flux surface for $\phi = \sum_{m,n}\phi_{mn}\exp(-im\theta - in\psi)$. One dominant toroidal harmonic is present $(n = 4)$ with a dominant poloidal harmonic $(m = 8)$ plus a few lower amplitude sidebands to produce the ballooning envelope. Figures 1(a)–1(e) are snapshots taken just before the saturation of the dominant mode.

The measured real frequency is $\omega_r = -0.06c_s/L_T$ and the growth rate is $\gamma = 0.03c_s/L_T$. The closest analytic theory for toroidal ITG modes, in terms of the assumed ordering, is the slab branch in the long wavelength limit [4] with $\omega \sim \omega_{ti} \sim \epsilon_T^{1/2}\omega_{*T_i}$, $k_\theta\rho_i \sim \epsilon_T^{1/2}$, and the approximate dispersion relation given by

$$\omega = \frac{v_{ti}}{qR_0}(7\sqrt{\pi})^{1/5}[(qk_\theta\rho_s)^2\hat{s}/\epsilon_T]^{2/5}e^{i7\pi/10}, \qquad (6)$$

which yields $\omega_r = -0.05c_s/L_T$ and $\gamma = 0.07c_s/L_T$. Comparisons with more detailed eigenmode calculations of Tang and Rewoldt [3] show agreement within 15% in terms of real frequency, growth rate, and mode structure. This dominant eigenmode grows linearly and saturates at a level of $e|\phi(r = r_0, \theta = 0, n = 4)|/T_e = 0.03$, which is in the range of the mixing length level $1/k_\perp L_T = 0.06$, where

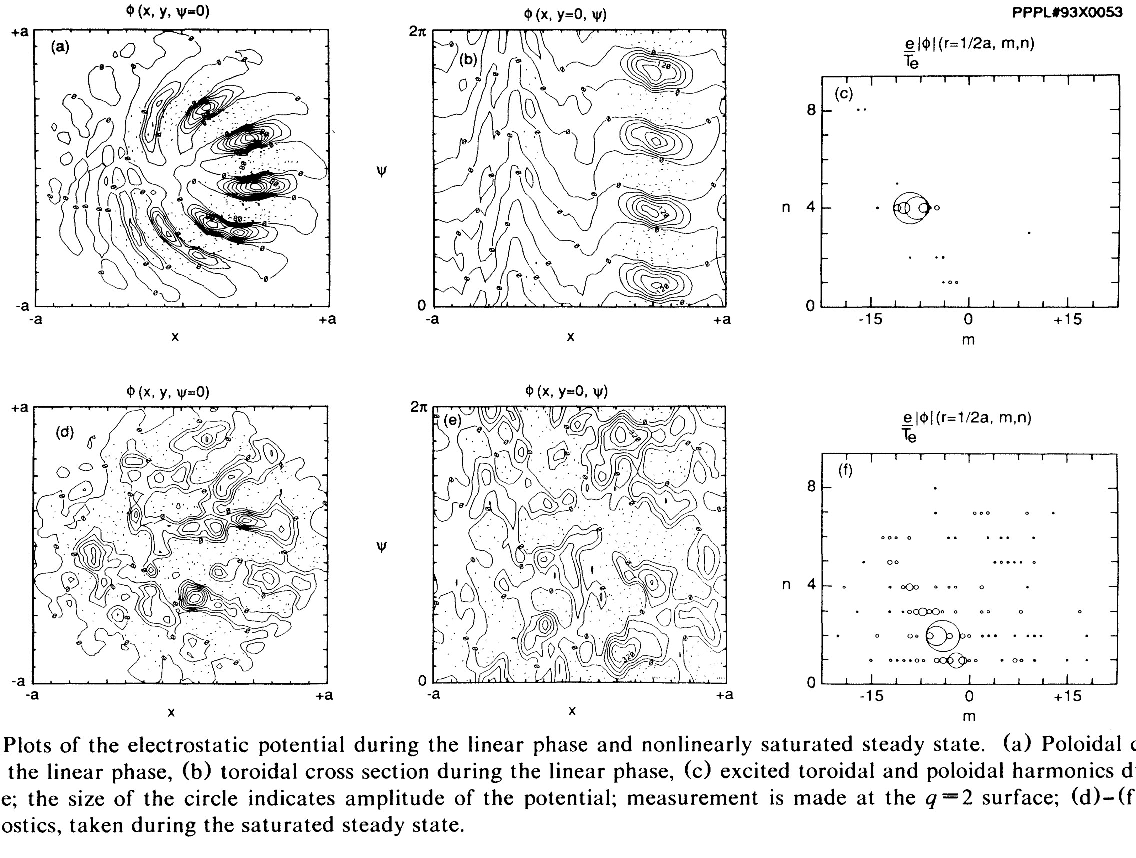

FIG. 1. Plots of the electrostatic potential during the linear phase and nonlinearly saturated steady state. (a) Poloidal cross section during the linear phase, (b) toroidal cross section during the linear phase, (c) excited toroidal and poloidal harmonics during the linear phase; the size of the circle indicates amplitude of the potential; measurement is made at the $q = 2$ surface; (d)–(f) are the same diagnostics, taken during the saturated steady state.

we use L_T since $1/L_n=0$ and $k_\perp \approx k_\theta$. The local 2D shearless slab mode coupling calculation [8] predicts a saturation level $e|\phi(x)|/T_e=\sqrt{3}|\omega+i\gamma|/k_\perp^2\rho_s c_s \approx 0.03$, which is in agreement with the toroidal simulation result. This may be due to the fact that the mode is not strongly localized radially. The toroidal mode coupling calculation will be investigated in the future; however, let us briefly comment on a plausible mechanism for the initial saturation of the most unstable mode. The linearly most unstable modes $(\pm l, \pm m, \pm n)$, where l is the radial mode number, couple together through the $\mathbf{E}\times\mathbf{B}$ nonlinearity to generate $(\pm 2l, 0, 0)$ temperature perturbations which then causes saturation, in a similar fashion as in Ref. [8]. At saturation, $\chi_i=1.6\rho_s^2 c_s/L_T$ taken at $r=r_0$, then drops and comes to a steady-state value of $\chi_i=0.2\rho_s^2 c_s/L_T$, for comparison $\gamma/k_\perp^2=0.5\rho_s^2 c_s/L_T$.

In the steady state, both long and short perpendicular wavelengths are enhanced with the spectrum peaking around $k_r\rho_s \sim 0$ and $k_\theta\rho_s \sim 0.1$–0.2, and the ballooning structure modified, but still prevalent. Broad scale (i.e., many modes are present) turbulence with a fluctuation level of $e|\phi_k|/T \lesssim 1\%$ is observed. Figures 1(d)–1(f) are the corresponding plots during the nonlinear saturated steady state. These snapshots were taken at a time $300 L_T/c_s$ after the saturation of the fastest growing mode. Figures 1(c) and 1(f) show the poloidal and toroidal harmonics (m,n) which have appreciable activity for the linear phase and the nonlinear state, respectively. After the system settles down to a steady state, the activity is at a lower (m,n) than the (m,n) associated with the most unstable mode. We also note that the peak of activity lies on the $m=qn$ line as expected.

Figures 2(a) and 2(b) are the k_θ and k_r spectra taken at the turbulent steady state. These measurements were made over the half annular region of $\theta \in [-\pi/2, +\pi/2]$, $r \in [\frac{1}{4}a, \frac{3}{4}a]$, and $\psi \in [-\pi, \pi]$. The region has approximately a $32\rho_s$ $(=a/2)$ radial width and a $100\rho_s$ $(=\pi a/2)$ poloidal length. Figure 2(a) shows $S(k_\theta) \equiv \sum_{n,k_r} |\phi(k_r,k_\theta,n)|^2$, and Fig. 2(b) shows $S(k_r) \equiv \sum_{n,k_\theta} |\phi(k_r,k_\theta,n)|^2$. These diagnostics are an attempt at mimicking the recent BES measurements on TFTR [5]. The spectrum shows similar features as the experimental measurements in that the k_r spectrum peaks at zero and k_θ spectrum peaks in the range of $k_\theta\rho_s \sim 0.1$–0.2. These properties of the spectrum have so far been found to be fairly insensitive to the choice of simulation parameters. One notable difference between the numerical result and the experimental measurement is that the width in the k_r spectrum is broader in the simulation. One possible explanation is the small minor radius of the simulation causes more localization of the modes radially, hence artificially broadening the k_r spectrum. This will be tested in the future, as the size of the simulations can be increased.

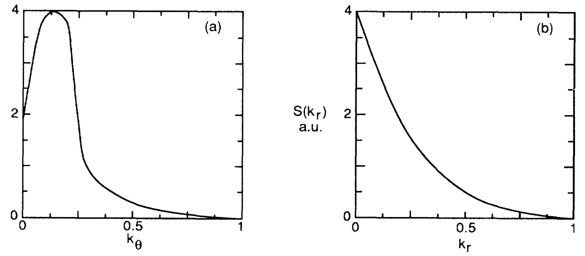

FIG. 2. Wavelength fluctuation spectra for k_θ and k_r. (a) Fluctuation amplitude vs k_θ and (b) fluctuation amplitude vs k_r. k_r and k_θ are in units of ρ_s^{-1}, and S is in arbitrary units.

Figure 3(a) shows the initial temperature profile (solid line) and the flattened profile in the quasisteady state (dashed line). The dashed line is measured at a time $750 L_T/c_s$ past the saturation of the most unstable mode, at which time the center temperature has dropped by 8%. The term quasisteady state is used because the temperature profile continues to relax at the transport time scale (approximately $a^2/\chi_i \sim 20\,000 L_T/c_s$), which is a much longer time scale than the initial transients (settling down before $300 L_T/c_s$), and the time scale of the ensuing fluctuations [approximately $(k_\parallel v_{ti})^{-1} \sim 30 L_T/c_s$]. To ensure this quasisteady state is still linearly unstable, we have made another run using the steady-state profile [shown in Fig. 3(a)] as an initial condition and observed comparable linear growth and nonlinear saturation. Note that the temperature relaxation is a global phenomenon and is not localized to any individual rational surface.

Figure 3(b) shows the radial variation in χ_i, which appears fairly flat, except towards the edge where χ_i goes to zero because the ion density fluctuations are set to zero in the simulation for $r \gtrsim a - 4\rho_i$. Simulations with larger volumes (i.e., a larger minor radius) will probably be needed to compare with the experimentally observed trends which show a radially increasing $\chi_i(r)$ profile [13].

Previous 3D sheared slab simulations have shown radial localization of the mode structure within a few ion gyroradii of the rational surface(s) [14]. For the 3D

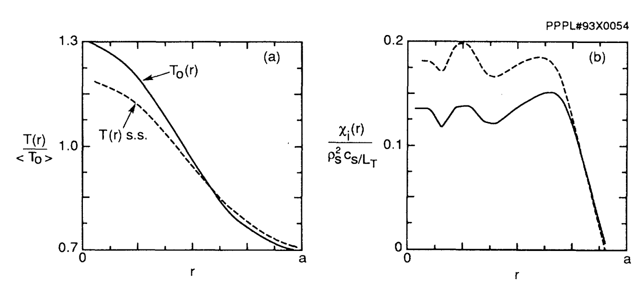

FIG. 3. Radial temperature profile and heat diffusivity. (a) Temperature vs radius; initial equilibrium is the solid line; dashed line is the steady state and (b) heat diffusivity χ_i vs radius at steady state; the solid line is χ_i calculated using initial equilibrium and the dashed line is calculated using the evolved equilibrium.

case, the resolved rational surfaces were closely spaced radially towards the center of the box, causing the fluctuations to be localized there as well, producing a relatively small steady state χ_i of approximately $0.004\rho_s^2 c_s/L_T$ [14]. The larger toroidal simulations presented here have more resolved rational surfaces which are distributed throughout the minor radius, producing a more turbulent system and a much larger steady-state heat flux. In addition, the toroidal case has a larger linear growth rate, and remnants of the radially elongated mode structure (toroidal coupling of the rational surfaces) persist in the turbulent steady state. It is interesting to note that on the strong B-field side ($\theta = \pm\pi$), the mode structure is more slablike, i.e., more localized to rational surfaces, which is consistent with 2D toroidal eigenmode calculations [3].

We have also run a case with the same parameters *except* for using a finite L_n, such that $\eta_i \equiv L_T/L_n = 2.3$, the purpose being to see the effect of running closer to marginal stability and compare with the unperturbed supershot parameters [12]. In this case ($\eta_i = 2.3$), the shape of the k_r, k_θ spectrum is similar, but the steady state χ_i is reduced to approximately $0.06\rho_s^2 c_s/L_T$. It is interesting to compare the simulation results to the thermal diffusivity in gyro-Bohm units for the perturbation experiment on TFTR [12], where both the perturbed and unperturbed cases gave $\chi_i \approx 0.3\rho_s^2 c_s/L_T$. The simulation gives good agreement for the flat density case (perturbed case); however, it shows a considerable reduction in the gyro-Bohm coefficient for the case closer to marginal stability ($\eta_i = 2.3$, unperturbed case) which was not observed in the experiment. This discrepancy may be in part due to a simplified physics model. Other effects found to be important, but are not included in our model, include trapped electrons, collisions, energetic ions, and impurities [8–10].

To gain some insight into the scaling trends of ITG driven transport, one can examine the invariance properties [15] of the governing equations. In the gyrofluid limit, the scaling can be written as [8]

$$\chi_i \propto (k_\perp \rho_s)^{-p} (\rho_s/L_T) cT/eB \,, \tag{7}$$

using $k_\parallel \approx 1/qR$ and $L_T/R = \text{const}$. Although the quasilinear theory gives $p = \frac{5}{3}$ [8], in general, the exponent p does not have a unique solution (because of the insufficient number of allowable transformations). Nevertheless, this scaling indicates that if the $k_\perp \rho_s$ spectrum in the turbulent steady state remains unchanged for different sizes of minor radius, a, the magnitude of χ_i should remain constant, which would give gyro-Bohm scaling. However, preliminary indications from larger simulations show that χ_i increases with system size. Thus, the scaling is not entirely gyro-Bohm. Furthermore, the simulation has a minor radius which is 5–10 times smaller in comparison with the TFTR experiments [5,12], and has a wider k_r spectrum and a smaller χ_i. These observations are evidence of non-gyro-Bohm scaling and the trend is consistent with Eq. (7). Recent dimensionless scaling experiments on TFTR [16] give the same non-gyro-Bohm trend.

In summary, our 3D toroidal gyrokinetic simulations confirm the radially elongated ballooning mode structure predicted by linear theory and show the nonlinear saturation of these toroidal modes. The ensuing turbulent spectrum retains remnants of the linear mode structure, and has similar features as recent experimental fluctuation measurements [5]. Current whole tokamak simulations are limited to minor radii of $(100\text{–}200)\rho_s$. In the future, teraflop scale massively parallel supercomputers will allow simulations with a minor radius in the range of $400\rho_s$, which is typical of the size of present day tokamaks. Such simulations will continue to serve as a useful tool for a better understanding of tokamak turbulence.

We thank L. Chen, J. Li, H. E. Mynick, G. W. Rewoldt, J. V. Reynders, W. M. Tang, and X. Q. Xu for helpful discussions. Computing was provided by Advanced Computer Laboratory, Los Alamos National Laboratory. This work was supported by U.S. Department of Energy Contract No. DE-AC02-76CHO-3073.

[1] S. E. Parker and W. W. Lee, Phys. Fluids B **5**, 77 (1993).
[2] A. M. Dimits and W. W. Lee (to be published).
[3] W. M. Tang and G. Rewoldt (to be published).
[4] F. Romanelli, L. Chen, and S. Briguglio, Phys. Fluids B **3**, 2496 (1991).
[5] R. J. Fonck *et al.*, Phys. Rev. Lett. **70**, 3736 (1993).
[6] T. S. Hahm, Phys. Fluids **31**, 2670 (1988).
[7] A. Thyagaraja and F. A. Haas, Phys. Scr. **47**, 266 (1993).
[8] W. W. Lee and W. M. Tang, Phys. Fluids **31**, 612 (1988).
[9] G. Rewoldt and W. M. Tang, Phys. Fluids B **2**, 318 (1990).
[10] X. Q. Xu and M. N. Rosenbluth, Phys. Fluids B **3**, 627 (1991).
[11] W. W. Lee, J. Comput. Phys. **72**, 243 (1987).
[12] M. C. Zarnstorff *et al.*, in *Proceedings of the 13th International Conference on Plasma Physics and Controlled Nuclear Fusion Research, Washington D.C., 1990* (International Atomic Energy Agency, Vienna, 1991), Vol. 1, p. 39.
[13] P. C. Efthimion *et al.*, Phys. Rev. Lett. **66**, 421 (1991).
[14] R. D. Sydora, T. S. Hahm, W. W. Lee, and J. M. Dawson, Phys. Rev. Lett. **64**, 2015 (1990).
[15] J. W. Connor and J. B. Taylor, Nucl. Fusion **17**, 1047 (1977).
[16] F. W. Perkins *et al.*, Phys. Fluids B **5**, 477 (1993).